Letter | Editors' Suggestion

Experimental realization of a rotating radio-frequency ion trap for precision metrology

Sun Yool Park,[1,*] Anzhou Wang,[1] Kia Boon Ng,[2] Patricia Hector Hernandez,[1] Addison Hartman,[1] Tuan Anh Nguyen,[1] Rohan Kompella,[1] Michail Athanasakis-Kaklamanakis,[1] Jun Ye,[1] and Eric A. Cornell[1]

[1]*JILA, NIST and University of Colorado, and Department of Physics, University of Colorado, Boulder Colorado 80309, USA*

[2]*TRIUMF, Vancouver, British Columbia V6T 2A3, Canada*

(Received 11 May 2026; accepted 24 August 2026; published 5 November 2026)

We discuss the experimental realization of a rotating radio-frequency (rrf) trap, proposed by Hasegawa and Bollinger [Phys. Rev. A **72**, 043403 (2005)]. Compared to a traditional linear rf (lrf) Paul trap, the rrf trap is a closer analogy to the popular mechanical lecture demonstration for a Paul trap. In an ion trap with realistic, nonideal electrode geometry, the rrf trap averages over angular variations in the effective potential. This averaging provides more uniform confinement and reduces ion loss compared with the lrf trap at equal trap strength near the center. This feature makes the rrf trap configuration advantageous for precision metrology applications, such as electron electric dipole moment (eEDM) measurements.

DOI: 10.1103/sxc6-199m

Introduction. Radio-frequency (rf), or Paul, traps allow for confinement in all three directions. Since three-dimensional ion confinement using purely electrostatic fields is not a solution of Laplace's equation, linear rf (lrf) ion traps utilize alternating confining and anticonfining potentials oscillating along the x and y axes as shown in Fig. 1(a). The rapidly oscillating fields drive micromotion, and this micromotion in the field gradient results in an effective secular confining potential. Since their introduction in the 1950s by Wolfgang Paul [1], lrf ion traps have been used in many applications, including quantum computation [2–7], atomic clocks [8–12], and physical chemistry [13–15].

A familiar Paul trap lecture demonstration is based on a rotating, saddle-shaped surface [16]. An object constrained to the surface by gravity and surface forces experiences a potential that rotates with time as in Fig. 1(b). About 20 years ago, Hasegawa and Bollinger proposed an analogous rotating rf (rrf) ion trap [17]. At the rf frequency, the conventional lrf potential flaps between two axes, whereas the rrf potential rotates. Prior to this work, no experimental realization of an rrf ion trap has been reported in the literature. This could be because an rrf ion trap is experimentally more complex, requiring multiple phases of rf voltages on multiple electrodes.

In this paper, we revisit this proposal and present an experimental realization of the rrf ion trap, verifying the predicted dynamics outlined in Ref. [17]. Furthermore, we demonstrate a practical advantage of the rrf trap for precision metrology: it reduces inherent trap-depth anisotropies in eight-rod trap geometries used for precision spectroscopy of trapped molecular ions.

*Contact author: sun.park@colorado.edu

Published by the American Physical Society under the terms of the Creative Commons Attribution 4.0 International license. Further distribution of this work must maintain attribution to the author(s) and the published article's title, journal citation, and DOI.

Our group at JILA recently constrained the electron's electric dipole moment (eEDM) to $|d_e| < 4.1 \times 10^{-30}\ e\,\mathrm{cm}$ using molecular ions in an lrf trap [18] and is attempting to further extend the precision [19,20]. Statistical sensitivity scales as $\sqrt{N\tau}$, where N is the number of detected ions and τ is the coherence time. Therefore, we aim to trap as many ions as possible while suppressing unwanted ion-ion interactions by adiabatically reducing the secular frequency, which lowers the ensemble temperature and density. We distinguish between the *tightness* of ion confinement proportional to the secular frequency at the trap center and the *effective depth* of the trap set by the total energy required to escape the trap via the lowest saddle point. While loose confinement can be advantageous for reducing interaction-driven decoherence, it also makes the ions more vulnerable to confining-potential inhomogeneity: the effective trap depth becomes shallower, which increases ion loss. The rrf trap mitigates this tradeoff by averaging over certain static inhomogeneities and anharmonicities, yielding a deeper effective trap depth for the same tightness of confinement.

Theory and experimental realization of the rrf trap

a. Idealized trap potentials. In an ideal lrf ion trap, an ion experiences a dc axial potential Φ_z and an oscillating radial quadrupole potential Φ_{lrf} given in cylindrical coordinates (r, θ, z) by

$$\Phi_z = -\frac{V_{\mathrm{dc}}}{r_{\mathrm{a}}^2}(r^2 - 2z^2),$$
$$\Phi_{\mathrm{lrf}} = \frac{V_{\mathrm{rf}}}{r_{\mathrm{r}}^2} r^2 \cos(2\theta)\cos(2\omega t), \tag{1}$$

where V_{dc} and V_{rf} are the dc and the rf voltages applied, r_{a} and r_{r} are effective axial and radial dimensions of the end caps and radial electrodes, and $2\omega = \omega_{\mathrm{rf}}$ is the rf frequency [17]. By contrast, in an rrf trap, the rf radial potential rotates with time as [17]

$$\Phi_{\mathrm{rrf}} = \frac{V_{\mathrm{rf}}}{r_{\mathrm{r}}^2} r^2 \cos[2(\theta + \omega t)]. \tag{2}$$

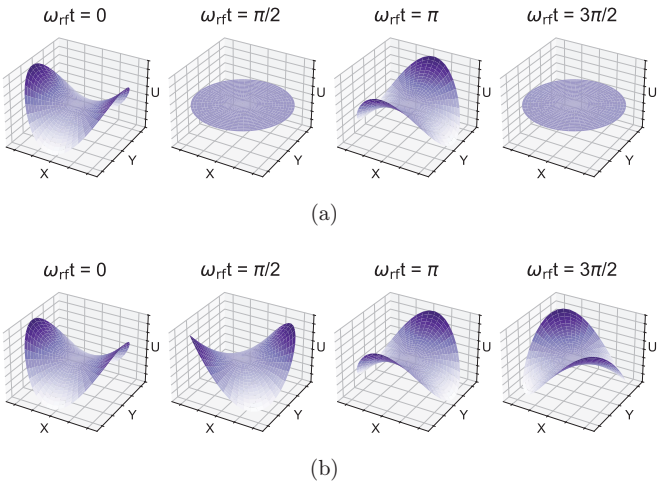


FIG. 1. The landscape of the oscillating component of the potential of (a) the linear rf ion trap and (b) the "mechanical" Paul trap at selected times. (a) The potential is confining (anticonfining) along the x-axis (y-axis) at $\omega_{\rm rf}t = 0$. A quarter period later, the potential landscape is flat. Half a period later, the potential flips its sign. The saddle flaps along the x and y axes. (b) The potential rotates. The same rotating pattern appears in the rrf ion trap.

The dimensionless Mathieu parameters q and d are defined as

$$q = \frac{4q_0V_{\rm rf}}{m_0{\omega_{\rm rf}}^2{r_{\rm r}}^2},$$
$$d = \frac{4q_0V_{\rm dc}}{m_0{\omega_{\rm rf}}^2{r_{\rm a}}^2}, \tag{3}$$

where q_0 is the charge of the ion and m_0 is the mass of the ion. The q parameter describes the strength of the rf electric field while d describes the applied dc quadrupole field.

Ion motion in an idealized lrf trap has been discussed extensively (see, e.g., Refs. [21,22]). For an rrf ion trap, Hasegawa and Bollinger solved the equations of motion in the rotating, time-varying potential in Ref. [17]. In both lrf and rrf traps in the small-q limit, the transverse motion separates into a fast micromotion at $\omega_{\rm rf}$ and a slower secular motion. In an ideal lrf potential of Eq. (1), the two transverse secular modes are degenerate, with the eigenfrequency $\omega_0 = (\omega_{\rm rf}/2)\sqrt{q^2 - d}$. One convenient basis for these degenerate modes is clockwise (CW) and counterclockwise (CCW) circular motion. In practice, however, static transverse stray fields (often well approximated by an $x^2 - y^2$ quadrupole term) lift this degeneracy and select two orthogonal linear normal modes, typically aligned close to the x or y axis, resulting in two distinct secular frequencies $\omega_x \neq \omega_y$. In this case, the mode axes are fixed in the laboratory frame, and generic excitations lead to beating between the two linear modes.

In the rrf trap, the degeneracy is lifted intrinsically by the rotating rf drive. For a finite value of q, the two transverse secular eigenmodes are split even in the absence of static transverse fields. To leading order in q, the CW and CCW eigenfrequencies are [17]

$$\omega_\pm \simeq \frac{\omega_{\rm rf}}{2}\left(\sqrt{q^2 - d} \pm \frac{q^2}{2}\right). \tag{4}$$

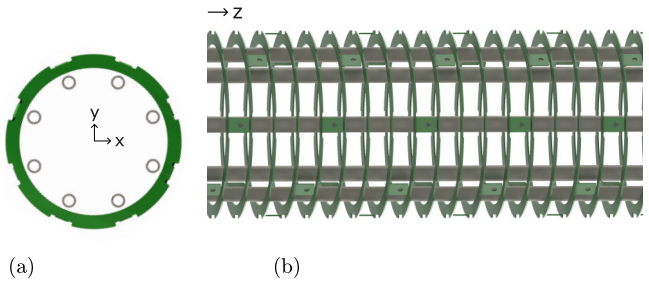


FIG. 2. Schematic of the trap. (a) Axial view of the electrodes and (b) side view of the electrodes. dc voltages are applied to the rings to produce the potential Φ_z approximated by Eq. (1) near the trap center. For ion detection, ejection voltages are pulsed onto the rings to accelerate the ions axially from the trapping region and onto an imaging ion detector, not shown. The rods provide radial confinement and the rotating polarizing electric field required for the eEDM measurement. For details of the electrode construction, see Refs. [19,23,24].

Because the rrf eigenmodes remain CW and CCW, a linearly polarized excitation along the x or y axis can be viewed as an equal-amplitude superposition of these eigenmodes. The resulting transverse motion stays linear, oscillating at $\bar{\omega}_{\rm sec} = (\omega_+ + \omega_-)/2$, but its axis rotates slowly in the xy plane at the precession rate $\omega_{\rm prec} = (\omega_+ - \omega_-)/2$. Exciting instead a pure CW or CCW mode produces a stable circular trajectory.

b. The JILA eight-rod trap. Figure 2 shows our trap geometry. A neutral beam of ThF arrives in a supersonic expansion with Ne and is ionized at the trap center by resonance-enhanced multiphoton ionization (REMPI), using schemes developed in Refs. [25–29]. At the end of an experiment, an axial field accelerates the ions toward a microchannel plate (MCP), reached after about 170 μs. Capacitive and phosphor-screen readouts provide the time-of-flight and radial profiles, respectively [30].

Unlike standard four-electrode lrf traps, our trap utilizes an eight-rod geometry to generate the highly uniform, rotating polarizing bias electric field necessary for our precision measurement. Each rod pair, comprising diametrically opposed rods, is driven separately, giving us full control of both amplitude and phase between rod pairs. Opposite rods are in phase for radial confinement and π out of phase for the polarizing field. A home-built direct digital synthesis system generates eight independently phase-controlled rf signals, one for each rod. Each signal is amplified through a resonant drive circuit [19,23]. The typical rf drive frequency is $\omega_{\rm rf}/2\pi = 50$ kHz, with a peak-to-peak amplitude of approximately 30 V.

c. Ion dynamics in the rrf trap. In our experiment, ions are excited with a relatively weak transverse electric field pulse along the x axis (or y axis), which prepares a linear superposition of the two circular eigenmodes within the harmonic region of the trapping potentials. The resulting transverse motion oscillates at $\bar{\omega}_{\rm sec} = (\omega_+ + \omega_-)/2$, with a slow precession at $\omega_{\rm prec} = (\omega_+ - \omega_-)/2$. Figure 3 shows that both $\bar{\omega}_{\rm sec}$ and $\omega_{\rm prec}$ vary with q in excellent agreement with Eq. (4). Equivalently, the transverse motion can be interpreted as that in an lrf trap in the presence of an effective axial magnetic field [17]. For a precession frequency of 200 Hz, the effective magnetic field is about 60 G for our ThF^+. dc potentials of the form

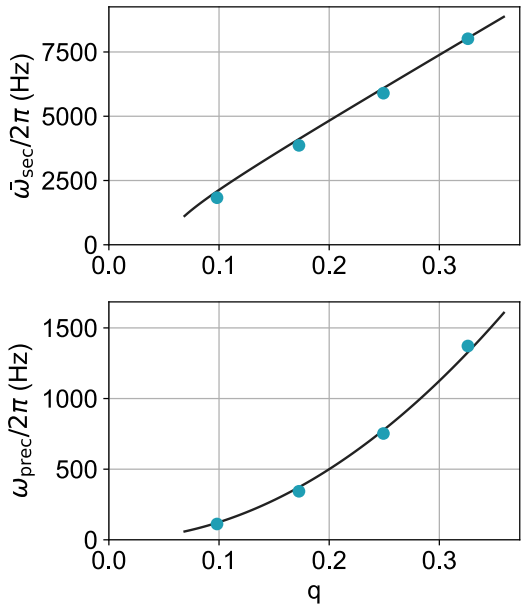


FIG. 3. Mean secular frequency $\bar{\omega}_{sec}$ (top) and precession frequency ω_{prec} (bottom) as a function of Mathieu parameter q, measured after a weak x-directed kick. Solid curves show Eq. (4), evaluated using calculated trap parameters with no fit parameters. Standard errors along either axis are smaller than the markers. Over this range, ω_{prec} is quadratic in q.

$x^2 - y^2$, unless shimmed away, can obscure magnetic-field- or rrf-induced CW/CCW splitting.

Figure 4 shows the transverse ion trajectory following an x-directed kick. Just before ejecting the ions for imaging, we quasiadiabatically ramp down the rf amplitude, suppressing the micromotion so that it is not visible in Fig. 4. The approximately 17-petal pattern is consistent with simultaneous

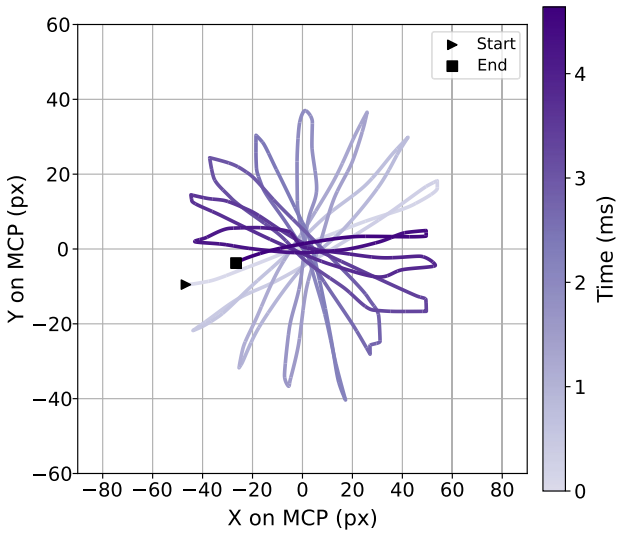


FIG. 4. Transverse ion trajectory beginning approximately 4 ms after an x-directed kick. Darker color indicates later detection. Lines connect successive points, and the data are smoothed with a three-point moving average. The y axis is stretched to reflect the 1.5:1 x-to-y magnification ratio of the imaging system.

CW and CCW excitation, with eigenfrequencies differing by about 12%. This corresponds to $\omega_{prec}/2\pi \approx 120$ Hz and $\bar{\omega}_{sec}/2\pi \approx 2000$ Hz and is different from the alternating linear and circular motion one observes in beating between $\hat{x}$ and $\hat{y}$ eigenmodes.

Implications for precision measurements in nonideal geometry

a. Pseudopotential in nonideal trap geometry. Our ion trap, as shown in Fig. 2, was carefully designed to provide a rotating polarizing bias electric field required for the eEDM measurement with 0.01% uniformity. However, it was *not* optimized to give perfectly harmonic rf confinement. To operate this eight-rod structure in a traditional lrf quadrupole configuration, the rods are driven with a phase pattern of $\{0, 0, \pi, \pi, 0, 0, \pi, \pi\}$. Because adjacent rods must be grouped in phase to approximate a four-pole geometry, this inherently produces a trap that is cylindrically symmetric only for small displacements. The anharmonic terms are highly anisotropic, characterized by a weak axis between adjacent electrodes held at the same instantaneous potential. When the trap confinement is loosened to minimize ion-ion interactions during precision spectroscopy, our ion cloud expands and samples regions where the fields deviate from the perfectly harmonic, idealized rf potentials discussed in the section *Theory and experimental realization of the rrf trap idealized trap potentials*. Instead of using the idealized rf potential, one can use a pseudopotential approximation to compute an effective potential. This approximation is widely used in rf trapping and is valid when the drive frequency is large compared to the secular frequencies and the micromotion amplitude is small on the spatial scale over which the field varies [21,22,31]. A convenient way of expressing the rf drive is

$$\mathbf{E}(\mathbf{r}, t) = \mathrm{Re}[\mathbf{E}_0(\mathbf{r}) e^{i\omega_{rf} t}],$$

where $\mathbf{E}_0(\mathbf{r})$ can be a complex spatial amplitude. In the pseudopotential approximation, the time-averaged micromotion leads to a time-independent effective potential that is proportional to the square of the rf field amplitude [22,31,32]

$$U_{ps}(\mathbf{r}) = \frac{{q_0}^2}{4 m_0 {\omega_{rf}}^2} \mathbf{E}_0(\mathbf{r}) \cdot \mathbf{E}_0(\mathbf{r})^* = \frac{{q_0}^2}{4 m_0 {\omega_{rf}}^2} |\nabla \Phi_0(\mathbf{r})|^2, \tag{5}$$

where $\mathbf{E}_0 = -\nabla \Phi_0$ and $\Phi(\mathbf{r}, t) = \mathrm{Re}[\Phi_0(\mathbf{r}) e^{i\omega_{rf} t}]$. With the rf drive $\mathbf{E}(\mathbf{r}, t)$ written in a complex form, it is clear that the pseudopotential approximation applies not only to the lrf potential, but also to the rrf potential where the difference between them is that the rrf potential has a complex amplitude $\Phi_0(\mathbf{r})$ with azimuthally varying phase. More specifically, the rrf potential of Eq. (2) can be written as

$$\Phi_{rrf}(r, \theta, t) \propto r^2 \cos(2\theta + \omega_{rf} t) = \mathrm{Re}[r^2 e^{i2\theta} e^{i\omega_{rf} t}].$$

With $\Phi_0(r, \theta) \propto r^2 e^{i2\theta}$, the corresponding pseudopotential is

$$U_{ps}(\mathbf{r}) \propto |\nabla \Phi_0|^2 = (|\nabla \Phi_c|^2 + |\nabla \Phi_s|^2), \tag{6}$$

where $\Phi_c \propto r^2 \cos(2\theta)$ and $\Phi_s \propto r^2 \sin(2\theta)$.

Using the pseudopotential approximation, the relevant measure of confinement and effective trap depth is the quantity $|\nabla \Phi_0|^2$. We now evaluate this quantity for our eight-rod geometry used in the experiment. We drive our eight radial

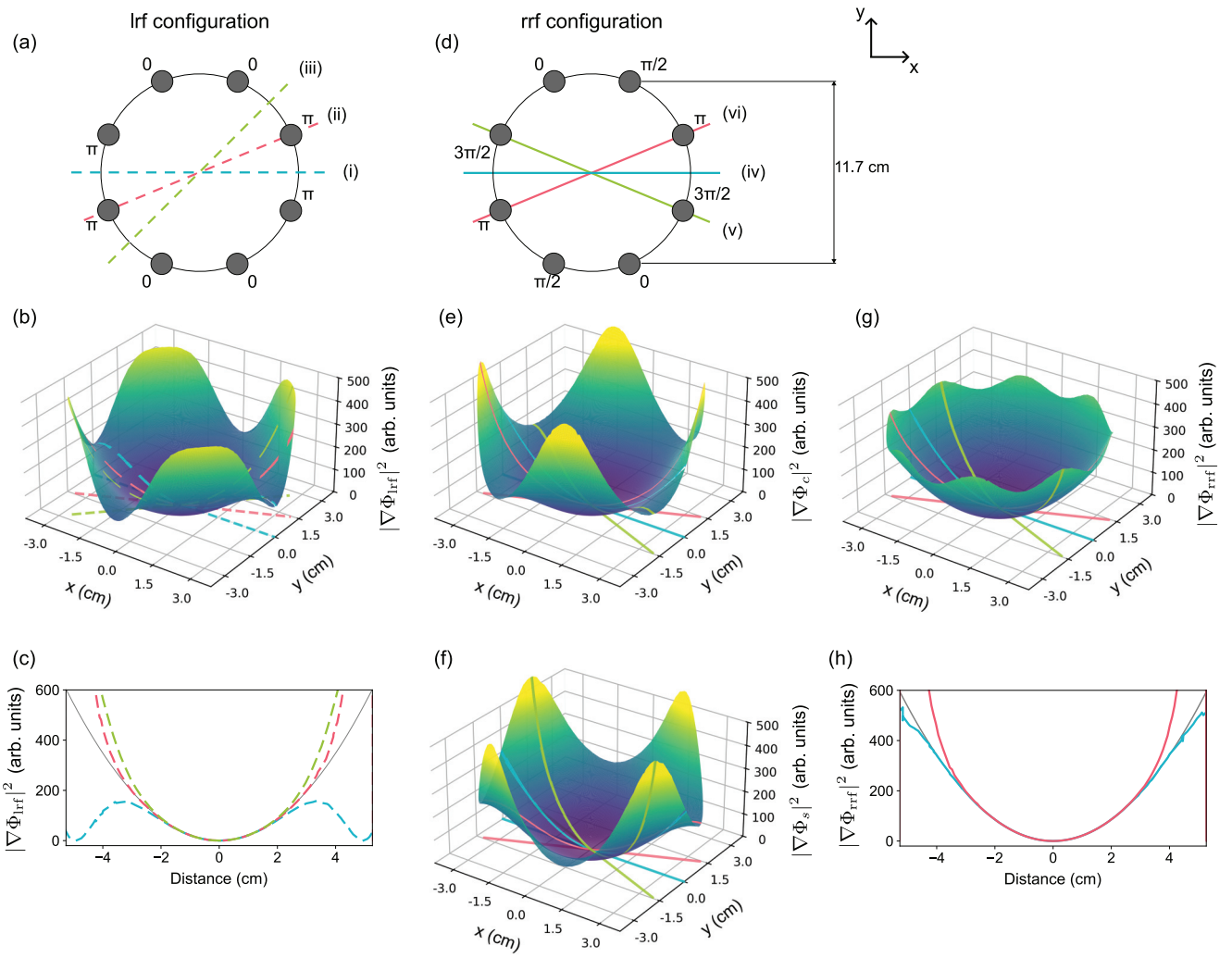


FIG. 5. Squared transverse rf-field amplitude, proportional to the pseudopotential $U_{\rm ps} \propto |\nabla\Phi|^2$, of the lrf and rrf trap configurations. (a) Electrode phase patterns and the three geometric cuts, labeled (i)–(iii), for the lrf configuration. (b) Surface plot of $|\nabla\Phi_{\rm lrf}|^2$ in the transverse plane. (c) Corresponding one-dimensional cuts along (i)–(iii). The grey curve shows a quadratic reference fit near the trap center. (d) Electrode phase pattern and the three geometric cuts, labeled (iv)–(vi), for the rrf configuration. (e) and (f) Surface plots of $|\nabla\Phi_c|^2$ and $|\nabla\Phi_s|^2$, respectively. (g) Average of the two quadratures as the total rrf field curvature $|\nabla\Phi_{\rm rrf}|^2 = (|\nabla\Phi_c|^2 + |\nabla\Phi_s|^2)/2$. (h) Corresponding one-dimensional cuts along (iv)–(vi). Note that the shallowest cut in this trap is deeper than that in the lrf trap.

electrodes with fixed phase offsets. For the lrf configuration the electrode phases are $\{0, 0, \pi, \pi, 0, 0, \pi, \pi\}$, while for the rrf configuration they are $\{\{0, \pi/2, \pi, 3\pi/2, 0, \pi/2, \pi, 3\pi/2\}\}$, as shown in Figs. 5(a) and 5(d), respectively. Figure 5(b) shows the transverse profile of $|\nabla\Phi_{\rm lrf}|^2$, a quantity to which the pseudopotential is proportional, for the lrf configuration. The effective trap depth is not azimuthally uniform and is shallowest along cut (i), which passes between the two electrodes held at the same instantaneous potential.

For the rrf configuration, as discussed above, the total pseudopotential can be decomposed into the cosine and sine quadratures, shown in Figs. 5(e) and 5(f), respectively. These two quadratures are related in space by

$$\Phi_c(r, \theta) = \Phi_s(r, \theta + \pi/4).$$

It is therefore tempting to think of the rrf pseudopotential as a simple azimuthal average of a single quadrature. However, the relevant quantity for the total pseudopotential is Eq. (6), the average of the two quadratures, and is shown in Fig. 5(g). Figure 5(h) shows the total rrf $|\nabla\Phi_{\rm rrf}|^2$ traces along the cuts. Because of the averaging over the two quadratures, the cuts at $\pm 22.5^\circ$ are identical, leaving only two unique traces. These traces are substantially more uniform than those of the lrf configuration in Fig. 5(c). More importantly, the shallowest direction in the rrf trap is deeper overall than in the lrf trap.

b. Enhancement of effective trap depth. To probe the predicted angular dependence of the trap depth, we adiabatically apply a static dipole field that adds an additional potential

$$U_{\rm dc}(\mathbf{r}) = -q_0 \mathbf{E}_{\rm dc} \cdot \mathbf{r},$$

which tilts the potential landscape. As $|\mathbf{E}_{\rm dc}|$ increases, ions are displaced from the trap center and eventually escape, so, by looking at how many ions survive as a function of tilt direction, we measure the direction dependence of the effective trap depth. We express the tilt as the harmonic equilibrium displacement $x_{\rm eq} \equiv q_0 E_{\rm dc}/(m\tilde{\omega}_{\rm sec}^2)$.

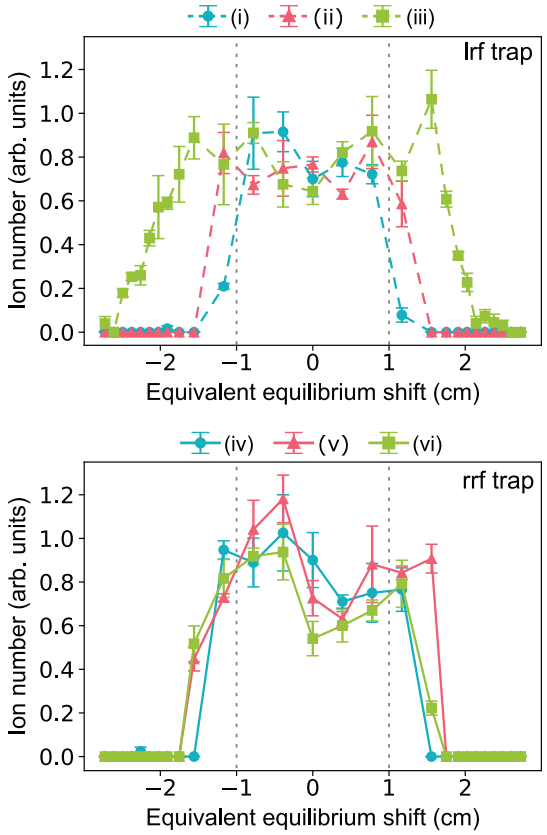


FIG. 6. Ion survival as a function of adiabatic dc tilt for different transverse cuts. In both panels, cuts (i)–(vi) correspond to the transverse directions defined in Fig. 5. The horizontal axis is the applied tilt expressed as an equivalent equilibrium shift $x_{\mathrm{eq}} \equiv q_0 E_{\mathrm{dc}}/(m\bar{\omega}_{\mathrm{sec}}^2)$. Error bars show standard errors. The dotted vertical lines are guides to the eye. Top: cuts (i), (ii), and (iii) of the lrf configuration correspond to azimuthal angles 0°, 22.5°, and 45°, respectively. Ion loss occurs at smaller $|x_{\mathrm{eq}}|$ for cut (i), consistent with this direction having the shallowest effective confinement. Bottom: cuts (iv), (v), and (vi) of the rrf configuration correspond to 0°, 22.5°, and −22.5°, respectively. The loss curves occur at more similar $|x_{\mathrm{eq}}|$ across angles, indicating a more azimuthally uniform effective trap depth in the rrf configuration.

In Fig. 6, in the lrf configuration, ion loss occurs at different x_{eq} for different azimuthal angles, indicating a strong angular dependence of the effective trap depth. By contrast, the rrf configuration effectively reduces this asymmetry down to just two distinct axes. Because the quadrature averaging maps the +22.5° and −22.5° directions onto the exact same averaged pseudopotential profile, the experimental loss curves for these two angles are very similar. Crucially, the absolute minimum $|x_{\mathrm{eq}}|$ required for ions to escape is noticeably larger than that of the weakest axis in the lrf configuration.

In our ion cloud, Coulomb interactions redistribute energy among translational degrees of freedom, leading to ions exploring a wide range of trajectories over time. As a result, long-time trap depth is governed by the lowest available escape barrier of the effective potential, not by a single trajectory. The anisotropy of the lrf configuration therefore introduces "easy escape" directions that reduce this minimum barrier and yield a comparatively shallow effective trap depth. By contrast, the rrf configuration raises this minimum barrier through quadrature averaging, resulting in a deeper overall trap depth.

Discussion. The eEDM sensitivity scales as $\sqrt{N}\tau$, with τ limited largely by ion-ion collisions and therefore by ion number, temperature, and confinement. The rrf trap offers one path towards deep but loose confinement. Other options include driving our eight rods in a hexadecapolar pattern to produce a potential closer to a square well. We are evaluating which approach is most promising for maximum eEDM sensitivity. Previous eEDM systematic studies assumed lrf confinement [33]. As discussed in the section *Ion dynamics in the rrf trap*, rrf secular motion is equivalent to lrf motion in an effective axial magnetic field of tens of gauss, at least 1000 times larger than the physical field used in the precision measurement. This fictitious field couples to center-of-mass motion, not directly to electron spins. However, its sign reverses with the rotation direction and therefore under time reversal. Because the eEDM search probes time-reversal violation, the systematic implications require careful study.

Acknowledgments. This work was supported by the Gordon and Betty Moore Foundation, Grant DOI 10.37807/GBMF13862, by the Alfred P. Sloan Foundation under Grant No. APSF 2025-79211, by AFOSR (Grant No. FA9550-20-1-0323), by NSF PFC (Grant No. PHY-2317149), by the National Institute of Standards and Technology, and by a Marsico Chair of Excellence. K.B.N. acknowledges support from the Banting Postdoctoral Fellowship No. BPF-198564, T.A.N. acknowledges support from the Hertz Foundation and from the NSF GRFP (Grant No. DGE 2040434).

Data availability. The data supporting the findings of this article are openly available [34].

[1] W. Paul and H. Steinwedel, Notizen: Ein neues massenspektrometer ohne magnetfeld, Z. Naturforsch. A **8**, 448 (1953), in German; often cited in English as "A new mass spectrometer without a magnetic field".

[2] J. I. Cirac and P. Zoller, Quantum computations with cold trapped ions, Phys. Rev. Lett. **74**, 4091 (1995).

[3] C. Monroe, D. M. Meekhof, B. E. King, W. M. Itano, and D. J. Wineland, Demonstration of a fundamental quantum logic gate, Phys. Rev. Lett. **75**, 4714 (1995).

[4] H. Haffner, C. Roos, and R. Blatt, Quantum computing with trapped ions, Phys. Rep. **469**, 155 (2008).

[5] R. Blatt and D. Wineland, Entangled states of trapped atomic ions, Nature (London) **453**, 1008 (2008).

[6] D. Main, P. Drmota, D. P. Nadlinger, E. M. Ainley, A. Agrawal, B. C. Nichol, R. Srinivas, G. Araneda, and D. M. Lucas, Distributed quantum computing across an optical network link, Nature (London) **638**, 383 (2025).

[7] M. Liu, R. Shaydulin, P. Niroula, M. DeCross, S.-H. Hung, W. Y. Kon, E. Cervero-Martín, K. Chakraborty, O. Amer, S. Aaronson, A. Acharya, Y. Alexeev, K. J. Berg, S. Chakrabarti, F. J. Curchod, J. M. Dreiling, N. Erickson, C. Foltz, M. Foss-Feig, D. Hayes, *et al.*, Certified randomness using a trapped-ion quantum processor, Nature (London) **640**, 343 (2025).

[8] S. A. Diddams, T. Udem, J. C. Bergquist, E. A. Curtis, R. E. Drullinger, L. Hollberg, W. M. Itano, W. D. Lee, C. W. Oates, K. R. Vogel, and D. J. Wineland, An optical clock based on a single trapped $^{199}Hg^{+}$ ion, Science **293**, 825 (2001).

[9] A. D. Ludlow, M. M. Boyd, J. Ye, E. Peik, and P. O. Schmidt, Optical atomic clocks, Rev. Mod. Phys. **87**, 637 (2015).

[10] M. C. Marshall, D. A. R. Castillo, W. J. Arthur-Dworschack, A. Aeppli, K. Kim, D. Lee, W. Warfield, J. Hinrichs, N. V. Nardelli, T. M. Fortier, J. Ye, D. R. Leibrandt, and D. B. Hume, High-stability single-ion clock with 5.5×10^{-19} systematic uncertainty, Phys. Rev. Lett. **135**, 033201 (2025).

[11] T. Lindvall, T. Fordell, K. J. Hanhijärvi, M. Doležal, J. Rahm, S. Weyers, and A. E. Wallin, $^{88}Sr^{+}$ optical clock with 7.9×10^{-19} systematic uncertainty and measurement of its absolute frequency with 9.8×10^{-17} uncertainty, Phys. Rev. Appl. **24**, 044082 (2025).

[12] C. Cheung, S. G. Porsev, D. Filin, M. S. Safronova, M. Wehrheim, L. J. Spieß, S. Chen, A. Wilzewski, J. R. C. López-Urrutia, and P. O. Schmidt, Finding the ultranarrow $^3P_2 \rightarrow {}^3P_0$ electric quadrupole transition in Ni^{12+} ion for an optical clock, Phys. Rev. Lett. **135**, 093002 (2025).

[13] S. Willitsch, Coulomb-crystallised molecular ions in traps: Methods, applications, prospects, Int. Rev. Phys. Chem. **31**, 175 (2012).

[14] B. R. Heazlewood, Cold ion chemistry within Coulomb crystals, Mol. Phys. **117**, 1934 (2019).

[15] O. A. Krohn and H. J. Lewandowski, Cold ion–molecule reactions in the extreme environment of a Coulomb crystal, J. Phys. Chem. A **128**, 1737 (2024).

[16] Harvard Natural Sciences Lecture Demonstrations, Rotating saddle, https://sciencedemonstrations.fas.harvard.edu/presentations/rotating-saddle, video accessed 2026-02-11.

[17] T. Hasegawa and J. J. Bollinger, Rotating-radio-frequency ion traps, Phys. Rev. A **72**, 043403 (2005).

[18] T. Roussy, L. Caldwell, T. Wright, W. Cairncross, Y. Shagam, K. B. Ng, N. Schlossberger, S. Y. Park, A. Wang, J. Ye, and E. A. Cornell, An improved bound on the electron's electric dipole moment, Science **381**, 46 (2023).

[19] K. B. Ng, The ThF^{+} eEDM experiment: Concept, design, and characterization, Ph.D. thesis, University of Colorado, Boulder, 2023.

[20] W. B. Cairncross and J. Ye, Atoms and molecules in the search for time-reversal symmetry violation, Nat. Rev. Phys. **1**, 510 (2019).

[21] D. Leibfried, R. Blatt, C. Monroe, and D. Wineland, Quantum dynamics of single trapped ions, Rev. Mod. Phys. **75**, 281 (2003).

[22] F. G. Major, V. N. Gheorghe, and G. Werth, *Charged Particle Traps: Physics and Techniques of Charged Particle Field Confinement* (Springer, Berlin, 2005).

[23] N. Schlossberger, An apparatus for measuring the electron's electric dipole moment in trapped ThF^{+}, Ph.D. thesis, University of Colorado, Boulder, 2023.

[24] S. Y. Park, Achieving long coherence time for a multiplexed, ion-based eEDM experiment, Doctoral thesis, University of Colorado, Boulder, 2026.

[25] H. Loh, J. Wang, M. Grau, T. S. Yahn, R. W. Field, C. H. Greene, and E. A. Cornell, Laser-induced fluorescence studies of HfF^{+} produced by autoionization, J. Chem. Phys. **135**, 154308 (2011).

[26] H. Loh, R. P. Stutz, T. S. Yahn, H. Looser, R. W. Field, and E. A. Cornell, REMPI spectroscopy of HfF, J. Mol. Spectrosc. **276–277**, 49 (2012).

[27] M. Grau, A. E. Leanhardt, H. Loh, L. C. Sinclair, R. P. Stutz, T. S. Yahn, and E. A. Cornell, Near-infrared LIF spectroscopy of HfF, J. Mol. Spectrosc. **272**, 32 (2012).

[28] D. N. Gresh, K. C. Cossel, Y. Zhou, J. Ye, and E. A. Cornell, Broadband velocity modulation spectroscopy of ThF^{+} for use in a measurement of the electron electric dipole moment, J. Mol. Spectrosc. **319**, 1 (2016).

[29] Y. Zhou, K. B. Ng, L. Cheng, D. N. Gresh, R. W. Field, J. Ye, and E. A. Cornell, Visible and ultraviolet laser spectroscopy of ThF, J. Mol. Spectrosc. **358**, 1 (2019).

[30] Y. Shagam, W. B. Cairncross, T. S. Roussy, Y. Zhou, K. B. Ng, D. N. Gresh, T. Grogan, J. Ye, and E. A. Cornell, Continuous temporal ion detection combined with time-gated imaging: Normalization over a large dynamic range, J. Mol. Spectrosc. **368**, 111257 (2020).

[31] A. V. Gaponov and M. A. Miller, Potential wells for charged particles in a high-frequency electromagnetic field, J. Exptl. Theor. Phys. **34**, 242 (1958) [Sov. Phys. JETP **7**, 168 (1958)].

[32] W. Paul, Electromagnetic traps for charged and neutral particles, Rev. Mod. Phys. **62**, 531 (1990).

[33] L. Caldwell, T. S. Roussy, T. Wright, W. B. Cairncross, Y. Shagam, K. B. Ng, N. Schlossberger, S. Y. Park, A. Wang, J. Ye, and E. A. Cornell, Systematic and statistical uncertainty evaluation of the HfF^{+} electron's electric dipole moment experiment, Phys. Rev. A **108**, 012804 (2023).

[34] S. Y. Park, Data supporting "Experimental realization of a rotating radio-frequency ion trap for precision metrology" [Dataset], Zenodo, 2026, doi: 10.5281/zenodo.22667780.